Revisiting the Determination of the Valence Band Maximum and Defect Formation in Halide Perovskites for Solar Cells: Insights from Highly Sensitive Near-UV Photoemission Spectroscopy

*Dorothee Menzel[†], Alvaro Tejada[†‡], Amran Al-Ashouri[†], Igal Levine[§], Jorge Andres Guerra[‡], Bernd Rech[ϑ+], Steve Albrecht[†+], Lars Korte[†]**

[†] Young Investigator Group Perovskite Tandem Solar Cells, Helmholtz-Zentrum Berlin für Materialien und Energie GmbH, Kekuléstraße 5, 12489 Berlin, Germany

[§] Helmholtz-Zentrum Berlin für Materialien und Energie GmbH, Kekuléstraße 5, 12489 Berlin, Germany

[‡] Departamento de Ciencias, Sección Física, Pontificia Universidad Católica del Perú, Av. Universitaria 1801, 15088 Lima, Peru

[ϑ] Helmholtz-Zentrum Berlin für Materialien und Energie GmbH, Scientific Management, Hahn-Meitner-Platz 1, 14109 Berlin, Germany

[+] Technical University Berlin, Faculty IV – Electrical Engineering and Computer Science, Marchstraße 23, 10587 Berlin, Germany

Keywords: halide perovskites, photoemission spectroscopy, near-UV spectroscopy, solar cells, defect states

1. Abstract

Using advanced near-UV photoemission spectroscopy (PES) in constant final state mode (CFSYS) with very high dynamic range, we investigate the triple-cation lead halide perovskite $Cs_{0.05}(MA_{0.17}FA_{0.83})_{0.95}Pb(I_{0.83}Br_{0.17})_3$ and gain detailed insights into the density of occupied states (DOS) in the valence band and band gap. A valence band model is established which includes the parabolic valence band edge and an exponentially decaying band tail in a single equation. This allows to precisely determine two valence band maxima (VBM) at different k-vectors in the angle-integrated spectra, where the highest one, resulting from the VBM at the R-point in the Brillouin zone, is found between – 1.50 eV to - 1.37 eV relative to the Fermi energy E_F. We investigate quantitatively the formation of defect states in the band gap up to E_F upon decomposition of the perovskites during sample transfer, storage, and measurements: During near-UV based PES, the density of defect states saturates at a value that is around four orders of magnitude below the density of states at the valence band edge. However, even short air exposure, or 3h of X-ray illumination, increased their density by almost a factor of six and ~ 40, respectively. Upon prolonged storage in vacuum, the formation of a distinct defect peak is observed. Thus, near-UV CFSYS with modelling as shown here is demonstrated as a powerful tool to characterize the valence band and quantify defect states in lead halide perovskites.

2. Introduction

Optoelectronic devices based on metal-halide perovskites (HaPs) have become a diverse field of research over the past decade. Prominent applications include light emitting diodes[1], single

junction solar cells[2] and top cells in tandem solar cells[3] (CIGS/perovskite,[4–6] silicon/perovskite[7,8] and perovskite/perovskite[9]), in which the community has achieved outstanding results. One of the main advantages of HaPs is the rather simple manipulation of their optical band gap, which has led to the investigation of a large variety of different perovskite compositions.[10] So called "triple cation" HaPs, with a combination of organic (methylammonium (MA) and formamidinium (FA)) and inorganic (Cs) cations and mixed halides, I and Br, have gained special interest due to their comparatively high stability and reproducibility,[11] as well as impressive power conversion efficiencies of 25.5 % in single-junction[12] and well over 29 % in perovskite/silicon tandem solar cells.[8]

Despite strong interest and notable achievements in optimizing the HaP absorber materials as well as the charge-selective contact layers, a detailed understanding of the energetics (band edge energies, band alignments) at surfaces and interfaces is still an area of ongoing research. For such materials, Ultraviolet Photoemission Spectroscopy (UPS) is a well-established tool to investigate electronic properties such as the work function and the energy position of the valence band maximum (VBM), i.e. quantities which determine in a first approximation the band line-up and charge carrier redistribution upon the formation of electronic interfaces. However, conventional UPS with He-I excitation at 21.2 eV is of very limited use when it comes to the characterization of occupied defect states in the band gap, between the VBM and Fermi energy. Standard UPS is only capable of measuring a density of states (DOS) 2-3 orders of magnitude lower than the valence band DOS, which is not sufficient to detect typical defect densities in the band gap of HaPs. Additionally, very careful analysis is needed to correct for existing satellite lines.[13] Due to the characteristically low DOS of HaPs at the VBM,[14] the correct evaluation of the valence band edge is particularly difficult. Occupied trap-states in the band gap have been observed before, e.g.

by Zhang et al.[15] and Wu et al.[16] using conventional He-UPS. However, the resolution is limited and a quantification not easily achievable.

In this work, we report on photoemission spectroscopy (PES) measurements with near-UV light excitation ($h\nu$ = 4-7 eV) to investigate the position of valence band features, electronic states in the exponential band tail and the density of occupied gap states of the triple-cation lead halide perovskite $Cs_{0.05}(MA_{0.17}FA_{0.83})_{0.95}Pb(I_{0.83}Br_{0.17})_3$ (CsMAFA). Recently, it has been shown that such near-UV PES with varying excitation energies from 3.8 eV to 7.7 eV is a powerful technique, capable of probing very low densities of gap states in bromide-rich wide band gap mixed halide perovskites.[17] However, in order to come to a *quantitative* measure of such densities of states, the variation of illumination intensity of commonly employed sources in this wide spectral range needs to be taken into account. This is done by calculating the photoelectron yield, i.e. the ratio of photoelectron count rate and absorbed photon flux. Combined with measuring the photoelectrons in constant final state mode, this technique is termed constant final state yield spectroscopy, CFSYS. It was first described by Sebastiani et al.[18] and then mostly applied to hydrogenated amorphous silicon (a-Si:H).[18,19] Here, we employ Near-UV CFSYS for the first time for a detailed investigation of CsMAFA valence band and the evolution of defect states. We demonstrate that with CFSYS, the DOS of HaPs can be measured over a very high dynamic range of up to seven orders of magnitude, which is four to five orders of magnitude below the noise level of typical He-UPS measurements and thus enables detection of both the valence band DOS as well as low defect densities in the band gap.

Determining the energetic position of the VBM for HaPs is however not straightforward and remains widely discussed.[14,20,21] Angle resolved PES measurements as well as DFT calculations of the dispersion relation of $MAPbI_3$ point to a strong dispersion of the energetically highest

valence bands.[21,22] Thus, when measuring angle integrated PES, it is challenging to correctly account for the very low DOS at the VBM, which is not located in the center of the Brillouin zone, but at the R-point in reciprocal space.[21–23] There are two main evaluation methods to obtain the VBM from valence band spectra measured by UPS found in literature: It is taken as the intercept of linear extrapolations of the leading edge of the energetically highest valence band feature and of the noise level, either a) on a linear ($E_{V,Lin}$), or b) on a semi-logarithmic ($E_{V,Log}$) scale. The former is the traditional approach for materials like Ge or GaAs[24], while the latter was first proposed by Endres et al. to account for the low DOS at the valence band onset.[14] This method circumvents the unphysically high values for the distance of E_V to the Fermi level, E_F, which sometimes even exceeds the known optical band gap, when using method (a). On the other hand, Yang et al. found that, by using method (b), the energetic position strongly depends on the applied UPS excitation energy.[21] They state that using method (a) on spectra recorded at the M-point and adding a fixed energetic distance to the R-point, known from DFT calculations, leads to the most reliable results.

We analyze our CFSYS spectra with a new band fluctuation model, which considers both the parabolic band edge(s) and the widely observed exponential band tail in a single expression.[25] With this, we evaluate the valence band maxima originating from different points in k-space, which are usually evaluated by angle-resolved measurements. The high resolution of our setup reveals several valence band maxima in one angle integrated spectrum. Furthermore, we investigate the influence of different sample histories, such as transfer through air or vacuum storage; exposure to UV light and X-rays during UPS/CFSYS and X-ray photoemission spectroscopy (XPS) measurements, on the density of occupied states in the HaP's band gap.

3. Experimental Methods

3.1 Sample Preparation

Glass substrates, fully covered with indium tin oxide (ITO, 15 Ω sq^{-1} sheet resistance), supplied by Automated Research GmbH, were first washed in an ultrasonic cleaner, subsequently in detergent (Mucasol), water, acetone and isopropanol and then cleaned using UV-O_3 just before the next preparation steps, which were conducted in an N_2-filled glovebox. For the hole-selective layer, a self-assembling monolayer (SAM) molecule, MeO-2PACz, was spin-coated at a concentration of 0.3mg ml^{-1} following a previously published procedure.[6] The perovskite precursor powders were dissolved in a 4:1 mixture of dimethylformamide (DMF) and dimethyl sulfoxide (DMSO), aiming for a perovskite precursor composition of $Cs_{0.05}(MA_{0.17}FA_{0.83})_{0.95}Pb(I_{0.83}Br_{0.17})_3$ (abbreviated as CsMAFA). The solution was spin-coated with a rotation speed of 3500 rpm (5 s acceleration, 35 s constant) and 250 µl Anisole was used as an antisolvent (drip 28 s after the start of spinning). The same perovskite has proven to be reproducible,[11,26] while showing a decent optoelectronic quality (~ 1 % photoluminescence quantum yield without further passivation). With C_{60} as electron transport layer and the exact same layer stack as investigated here, power conversion efficiencies of ~21 % for single junction solar cells were shown on SAMs,[6] and a similar formulation with slightly higher Br amount has been used in the record 29.2 %-efficient perovskite/silicon tandem solar cell.[8] While lower-bandgap perovskite composition due to its good batch-to-batch reproducibility and widespread use in multiple laboratories, with most of them yielding fairly similar results.

The layer stack for the investigated sample series is depicted in Figure 1. Each sample was transferred into the PES vacuum setup using an inert transfer unit filled with dry, pure nitrogen and has hence not been exposed to ambient atmosphere at any time. PES measurements were

started directly after transferring the samples into the vacuum system as soon as the necessary base pressure (<10^{-9} mbar) was reached. For the measurement, the sample was electrically grounded by two metal contacts which were pressed onto the ITO at the edge of the sample, where the perovskite had been scratched off beforehand. The ITO substrate assists here for lateral charge transport and ensures that severe charging effects can be excluded.

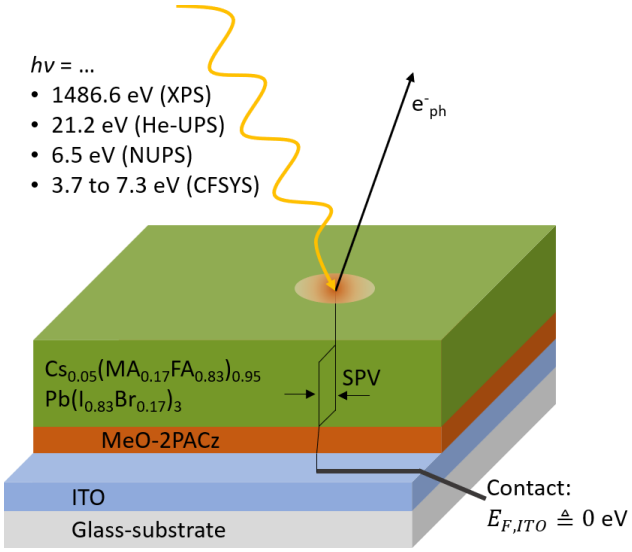

Figure 1. Schematic of the device stack with ITO/glass substrates, MeO-2PACz as hole selective monolayer and spin coated $Cs_{0.05}(MA_{0.17}FA_{0.83})_{0.95}Pb(I_{0.83}Br_{0.17})_3$ halide perovskite. Photoemission measurements were performed with different excitation energies. The samples were contacted via the ITO substrate, i.e. with $E_{F,ITO}$ as reference for the binding energy scale at $E_B = 0$ eV

3.2 Characterization methods

The PES measurements were carried out at a base pressure of < 10^{-9} mbar with three different excitation sources: near-Ultraviolet Photoemission Spectroscopy using a Xenon gas discharge lamp and double grating monochromator (NUPS, $h\nu = 6.5$ eV), Ultraviolet Photoemission Spectroscopy with a Helium discharge lamp (He-UPS, $h\nu = 21.2$ eV) and X-Ray Photoemission Spectroscopy with Al-K_α radiation (XPS, $h\nu = 1486.6$ eV at 400 W). Furthermore, Constant Final

State Yield Spectroscopy (CFSYS) with the broad spectrum of the Xenon gas discharge lamp (3.7 to 7.3 eV) in combination with a double grating monochromator was performed.

To minimize the possible light-induced degradation of the samples, a strict sequential order of measurements was pursued: 1. NUPS (illumination time, $t_{ill.} \approx 15$ min), 2. CFSYS ($t_{ill.} \approx 3$ h), 3. He-UPS ($t_{ill.} \approx 40$ min) and 4. XPS ($t_{ill.} \approx 3$ h). The measurement induced damage will be investigated in the results section. Note that, due to the necessary initial NUPS measurement, all CFSYS spectra were taken on samples that had been exposed to 15 min of UV-illumination, and had not been exposed to ambient air, unless stated otherwise. All methods share the same hemispheric electron energy analyzer EA-10 P, fabricated by SPECS.

The Xe-lamp can provide a sufficient and stable photon flux (> 10^{11} photons s^{-1} cm^{-2}) up to a photon energy of ~7 eV. The count rate of the photoelectrons, $n_{el}(E_{kin}, h\nu)$ is measured in the electron analyzer, with an energy resolution set to 125 meV. First, NUPS measurements with an excitation energy of $h\nu = 6.5$ eV were conducted to determine the secondary electron cut-off (SECO) and thus the work function of the specific layer. The final state kinetic energy for the CFSYS measurement is then chosen around 0.2 eV above the work function of the specific layer. The incident illumination photon flux, $n_{ph,i}$, and the photon flux reflected by the sample surface, $n_{ph,r}$, thus the reflectivity, R, are monitored by two calibrated silicon photodiodes. From these quantities, the internal photoelectron yield, Y_{IN}, i.e. the ratio of detected photoelectrons per absorbed photon, can be calculated. Y_{IN} generally depends on the kinetic energy of the photo electrons, E_{kin}, and the incident photon energy, $h\nu$:

$$Y_{IN}(E_{kin}, h\nu) = {}^{n_{el}}/_{(1-R)n_{ph,i}} \qquad (1)$$

Following the approach by Winer and Ley, we assume a constant dipole transition matrix element in the small energy range covered here and measure the photoelectrons at one constant

final state (E_{kin}^{0}= const), Y_{IN} is directly proportional to the number of occupied states, N_{occ}.[27] This is a rather strong assumption, which we will discuss this in more detail during the interpretation of modelled densities of states. Note, that the measured DOS does not depend on the conduction band structure anymore, which is an important advantage of CFSYS:

$$Y_{IN} \propto h\nu \cdot N_{occ}(E_{kin}^{0} - h\nu). \quad (2)$$

The incident photon flux on the sample for the standard slit width of the double grating monochromator at 2 mm varies with the chosen photon energy from $n_{ph,i} = 8 \cdot 10^{11}$ photons s^{-1} cm^{-2} at around $E_{ph} = 6.7$ eV to almost $n_{ph,i} = 5 \cdot 10^{13}$ photons s^{-1} cm^{-2} at $E_{Ph} = 3.7$ eV (see supporting information, Figure S1a and b).

3.3 Valence band modelling of CFSYS data

The strong dispersion and "soft" onset of the valence band signal in UV photoelectron spectra measured on HaPs[14] requires careful modelling of the valence band region. To this end, we adapted a model initially published by Guerra et al.[25,28] for optical absorption measurements. It assumes parabolic band edges and their energetic fluctuation due to varying local disorder. Structural and/or dynamic disorder induces exponential band tail states, also known as Urbach tails, which are observed in the band edge of all materials. The inverse of the exponential slope is defined as the Urbach energy, in agreement with universally observed Urbach rule.[29] In He-UPS measurements on HaPs, a similar exponential region has been found at the top of the valence band region.[14,23] Since there are fundamental differences between optical absorption measurements and near-UV PES methods, we define a more general parameter to describe the slope of this exponential tail caused jointly by the structural disorder and integration of the dispersion relation over the whole Brillouin zone, E_t.

Our model describes the density of occupied states, N_{OCC}, in dependence of the binding energy, E_B, and is based on a ½-degree polylogarithm function, $\mathrm{Li}_{1/2}$, with only three fitting parameters: the valence band edge ($E_{V,PLog}$), the inverse slope of the exponential band tail (E_t) and an arbitrary amplitude scaling parameter (a_0),

$$N_{OCC}(E_B) = -\frac{a_0}{2}\sqrt{E_t}\,\mathrm{Li}_{1/2}\left(-\exp\left(\frac{-E_B+E_{V,PLog}}{E_t}\right)\right). \quad (3)$$

Note, that such parameterizations of the valence band/tail region are often divided in two separate equations, being the assumed linear valence band edge and the exponential Urbach tail.[30] Our model describes both the parabolic and band tail region consistently in one single equation, without relying on arbitrary continuity conditions to join the two. For binding energies far below the valence band edge, $E_B << E_{V,PLog}$, it reproduces the conventional models for a square root DOS in the valence band, and for $E_B >> E_{V,PLog}$ an exponential tail into the band gap. See Guerra et al. for a more detailed mathematical discussion of the model.[25]

We modeled the measurements with a linear combination of 1) two Polylogarithm functions $N_{OCC,1} + N_{OCC,2}$ according to Eq. 3 representing two parabolic band edges and corresponding to two different parabolic VBM in reciprocal space ($E_{V,PLog,Low}$ and $E_{V,PLog,High}$, see the discussion section). $E_{V,PLog,Low}$ and $E_{V,PLog,High}$ then describe the respective valence band maxima and their amplitudes are fitted independently of each other. Here, E_t of both valence bands, are assumed equal since both parabolic band edges experience the same fluctuation broadening. 2) Three Gaussian functions (as commonly assumed for localized defect bands[19]) are used for modelling the occupied gap states in the band gap. All three defect bands are assumed to have the same *FWHM*, while the energetic position, E_{Di}, and the amplitude a_{Di} were free fitting parameters. The fitting parameter of the defect amplitude can easily be converted into the area under the Gaussian ($A_{Di} = a_{Di} \cdot FWHM \cdot \sqrt{\pi/(4\ln(2))}$). Those two general parts of the model are convolved with

the Fermi distribution at 298 K, with E_F also as a free fitting parameter with an upper limit of + 0.2 eV relative to the reference Fermi level $E_{F,ITO}$.

For the least-square fitting routine of the combined model to the measured DOS by CFSYS, the instrumental broadening needs to be considered, which is ensured by the convolution of the model function with the instrument transfer function as described in detail by Korte.[31]

4. Results and Discussion

We divide our results into three parts. First, we compare the valence band spectra measured by He-UPS, NUPS and CFSYS and use well established methods for a first evaluation of the VBM region. Afterwards, we provide a quantitative analysis of these CFSYS spectra by applying the model introduced in the previous section for fitting the VBM region and gap state density of our CsMAFA films, and discuss its physical interpretation. In the last section, we investigate possible degradation effects induced by the UV and X-ray illumination during measurements and different sample environments, and quantify the increase of deep gap states.

4.1 Comparing different UV photoemission spectroscopy modes

Figure 2 shows a comparison of He-UPS, NUPS and CFSYS measurements of the valence band region of a CsMAFA metal-halide perovskite layer, plotted on a semilogarithmic scale. For the NUPS and CFSYS spectra, the measured internal yield, Y_{IN} (left), is shown whereas the ordinate of the He-UPS spectrum (right) was scaled such that the spectrum fits with the other two measurements in the VB region at binding energies between -2.2 and -1.4 eV.

The first main advantage of the near-UV PES techniques (NUPS and CFSYS) is the high signal to noise ratio. A density of occupied states in the valence band at E_B = -2 eV of roughly $N_{OCC} = 10^{21}$ cm^{-3}eV^{-1} is obtained from the comparison to DFT calculations for $MAPbI_3$ by Shirayama et al..[22] We further calculate estimates for the detection limit of the respective methods

at $N_{OCC} \approx 10^{19}$ cm^{-3}eV^{-1} (He-UPS), 10^{16} cm^{-3}eV^{-1} (NUPS) and 10^{15} cm^{-3}eV^{-1} (CFSYS). The shown He-UPS data is corrected for the three main He-I satellite lines, similar to the procedure shown by Zhang et al.[13] The relative contributions to the measured sum spectrum due to the satellite lines can be determined by measuring e.g. the Fermi edge of a gold film. Since the exact intensity of the signal excited by the satellites might vary slightly depending on the material, due to different cross sections, the correction in practice is mostly done by manually adjusting the relative intensities of the satellite lines, which is prone to over- or underestimation. Hence, in conventional UPS gap states and even the exponential tail region are difficult to distinguish from residuals of this correction. In contrast to that, the double grating monochromator used for NUPS and CFSYS provides a single band of monochromatic light, which makes any further data processing unnecessary.

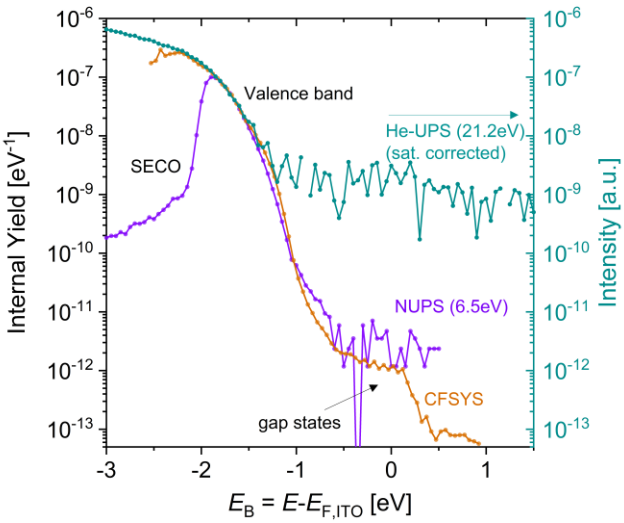

Figure 2. Valence band spectra of a metal-halide perovskite layer ($Cs_{0.05}(MA_{0.17}FA_{0.83})_{0.95}Pb(I_{0.83}Br_{0.17})_3$). Comparison of the occupied states in the valence band region using three different PES methods: 1. Turquoise, right ordinate: UPS with He-I-excitation ($h\nu = 21.2$eV), 2. Purple: NUPS with monochromatized Xe-lamp at $h\nu = 6.5$eV and 3. Orange: Constant Final State Yield Spectroscopy (CFSYS).

Using near-UV light for the photoemission process implies a second advantage of NUPS and CFSYS over conventional He-UPS: the information depth of PES depends primarily only on the

kinetic energy of the photoelectrons, which follows the so-called “universal curve” for the mean free path length.[32] While He-UPS is limited to photoelectrons from the first monolayers up to ~ 0.5 nm, with near-UV excited photoelectrons, the escape depth increases up to ~ 5 - 10 nm. In principle, this even permits directly investigating buried interfaces, which are usually only accessible with hard X-Ray PES.

The determination of a consistent VBM position for HaPs is widely discussed in literature.[13,14,33] The two most applied evaluation methods (intercept between linear fit and noise on either linear or semi-logarithmic scale) are compared in Figure 3a-c for our different PES methods.

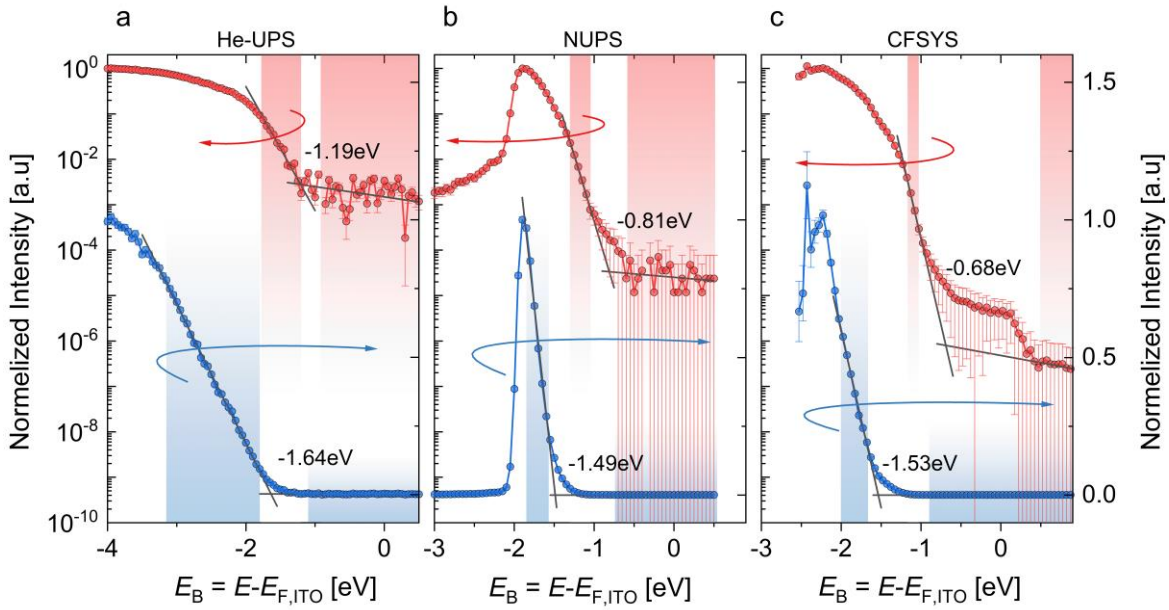

Figure 3. Example for the VBM evaluation for a metal-halide perovskite ($Cs_{0.05}(MA_{0.17}FA_{0.83})_{0.95}Pb(I_{0.83}Br_{0.17})_3$) on fully covered ITO/glass substrate: Normalized intensity (left semi-logarithmic, right linear scale) as function of binding energy for a) satellite-corrected He-UPS, b) NUPS (6.5 eV) and c) CFSYS measurements. The VBM is obtained as the intercept of the leading edge of the spectrum with the background: Both the VBM and the background are fitted with linear models, either on a semi-logarithmic (red, top) or a linear (blue, bottom) scale. The red and blue shaded areas indicate the data fitting regions used for the fits on the semi-logarithmic or the linear scale, respectively.

Extrapolating the DOS on a semi-logarithmic scale gives greater weight to the characteristically low DOS at the VBM (which in HaPs is found not to be located at the origin of the Brillouin zone)

and therefore also leads to energetically higher VBM positions. Zu et al. compared ARPES measurements with angle integrated He-UPS measurements, supported by DFT calculations on $MAPbI_3$. They evaluated the valence band spectra on a linear scale at different points in the Brillouin zone. Comparing them with VBM positions extracted on a semi-logarithmic scale from angle integrated UPS on thin films, they find good agreement between both methods.[23] However, as discussed in more detail below, this exponential tail is caused by the specific shape of the dispersion relation between the highest VBM and the lower lying bands in the valence band region.

Figure 3b and c show the VBM measured with NUPS and CFSYS (on the same sample as Figure 3a), and exemplary fits on a linear and semi-logarithmic scale similar to the He-UPS evaluation. Indeed, as also found by He-UPS, we observe a long exponential tail over roughly two orders of magnitude, but by decreasing the detection limit using NUPS and CFSYS, we reveal that the noise level of He-UPS intersects with this low DOS at an arbitrary energetic position. However, it is obvious that a consistent determination of the energetic position of the VBM should not depend on the measurement technique, as also suggested by Yang and Yang.[21] Additionally, the modelling of the noise itself by an exponential function is not justified by any physical reason.

Comparing the results on the linear and the semi-logarithmic scale, we find more consistent values in between the different measurement techniques by fitting on a linear scale, as also found by Yang and Yang.[21]

It can be seen that as the signal-to-noise ratio increases from the He-UPS to NUPS and CFSYS, $E_{V,Log}$ approaches the Fermi level. Measured with He-UPS (and corrected for satellite lines), the valence band maximum is found at $E_{V,Log}$ = -1.19 eV. With NUPS, and thus intermediate signal-to-noise ratio, $E_{V,Log}$ = -0.81 eV is found, and using CFSYS yields by far the energetically highest VBM position at $E_{V,Log}$ = -0.68 eV. With a perovskite band gap of 1.63 eV the latter value would

indicate a slight p-type character of the surface. Evaluated on the linear scale, the deviation between the fitted VBM positions is much smaller with ~ 150 meV in between the different measurement techniques. Comparing both evaluation methods on a linear and semi-logarithmic scale for CFSYS, a difference of 850 meV is found which is quite tremendous and would result in completely different interpretations of the doping-type of the material.

The same trend can be observed for four different, but nominally similar processed samples (supporting information, Figure S2 and Figure S3). The slight variation of the Fermi-level position in the band gap will be discussed in the next section.

In practice, the arbitrarily defined $E_{V,Log}$ found by evaluating He-UPS on the semi-logarithmic scale matches quite well with E_V obtained from more advanced angle-resolved PES. However, the mentioned inconsistencies demonstrate clearly, that a more elaborated modelling of the valence band maximum including a physical interpretation of the fitted parameters is required, which we will provide in the next section.

4.2 Combined modelling of valence band maxima and exponential band tail

The large spread in E_V values found in the previous section calls for a reliable model to describe the valence band structure and to consistently quantify the energetic position of the respective band edges. Figure 4a shows an exemplary valence band DOS of a CsMAFA thin film, measured by CFSYS. We propose a new model to describe the density of occupied states, N_{OCC}, and fit it to the measured internal yield. A detailed description can be found in the experimental section. The model basically consists of a polylogarithm function (blue line, 'VBM, PLog, High') and trap states, modeled tentatively by three Gaussian functions (D1-D3). These peaks only serve to extend the modelled DOS into the band gap and to include the trap states in the model in a physically meaningful way. For the sake of completeness, the modelled parameters are shown in the

supporting information (Table S1). The data here is normalized to the amplitude scaling parameter of the respective band edge, a_0. Note, that the actual N_{OCC} (red line) is broadened by the transfer function of the PES setup, resulting in the convolved DOS (black line).

As mentioned above, the model assumes parabolic band edges, which lead to a square root energy dependence of the N_{OCC}, in combination with an exponential band tail described by the slope parameter E_t.

The full model also includes the Fermi distribution, which cuts off the spectrum at the Fermi energy. However, for some samples, a reliable fit of the Fermi edge to the measured data is not possible, even though it is included in our model: For samples with low defect densities, the gap state density at the Fermi-edge is close to the detection limit and can thus not always be fitted consistently. Occasionally, the fit converges to modelling the drop of the DOS, which is actually attributed to the Fermi edge, instead as the high-energy side of the defect Gaussian D3. Therefore, we additionally fitted a sigmoidial Boltzmann function to the Fermi edge and report the obtained values as E_F^* as shown in Figure S4 and use this as consistent reference position.

For $E << E_{V,PLog,High}$ the measured data clearly exceeds the modelled DOS. We account for this by a second polylogarithm function as shown in Figure 4b, which can be attributed to the energetically next lower VBM in the dispersion relation. Further, the (unoccupied) conduction band is indicated as a guide to the eye by adding another polylogarithmic function at an energetic distance of 1.63 eV, corresponding to the optical gap as measured by UV-Vis spectroscopy, and with a tail parameter of 15 meV and thus close to the Urbach energy.

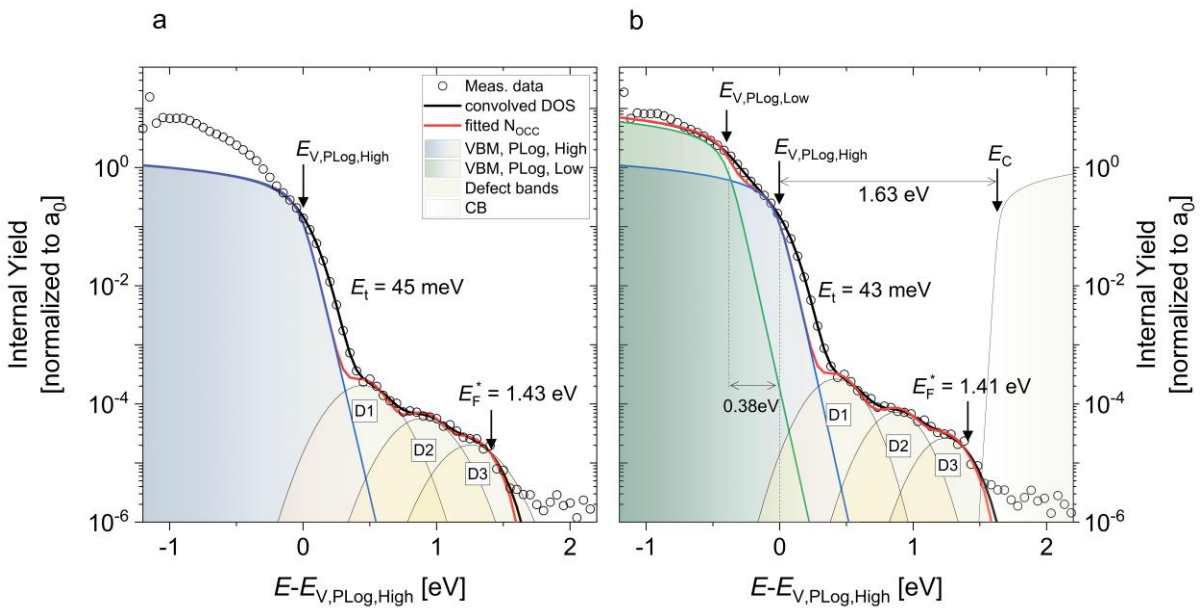

Figure 4. Internal yield of $Cs_{0.05}(MA_{0.17}FA_{0.83})_{0.95}Pb(I_{0.83}Br_{0.17})_3$ as measured by CFSYS. Modelling of the highest observed valence band edge(s) by a) one parabolic band edge ($E_{V,PLog,High}$) with an exponential tail (slope = $1/E_t$), jointly described by a polylogarithm (PLog) function and b) two PLog functions belonging to two different transitions in *k*-space. The gap state density is modeled by three Gaussian functions. The data was fitted with this model DOS convolved with the instrumental broadening of the PES set-up, and $E_{V,PLog,High}$ is chosen as the origin of the energy axis.

The Urbach energy can be evaluated by a linear fit on a semi-logarithmic scale of the sub-bandgap absorption measured by various methods, which are usually based on optical spectroscopy. HaPs are well known to show low Urbach energies below 16 meV.[34] For the herein used composition 15.5 meV was found by measuring external quantum efficiency[6] (EQE) and 14.3 meV by calculating the absorptivity from photoluminescence (PL) (see Figure S5) following a procedure as by Ledinský et al..[34] To justify the suitability of our model for quantifying the band tail slope, we modeled the absorption calculated from the complex refractive index, $\tilde{n}$, measured by spectroscopic ellipsometry (SE) and spectral transmittance (T), with the same polylogarithm model as by Guerra et al..[25] We found 15.3 meV as tail parameter (see Figure S6), which again, is in good agreement with the previously mentioned methods. In previous studies on hydrogenated

amorphous silicon, it has been shown, that CFSYS serves as reliable method to quantify the Urbach energy, yielding values in good agreement with literature.[19]

However, the band tail slope, E_t, which we observe in all our PES data is around 40-50 meV and hence over three times higher compared to the Urbach energy measured by sub-bandgap absorption spectroscopy methods. There are three principal differences of those methods compared to NUPS and CFSYS which need to be considered when comparing both tail parameters: i) PES is very surface sensitive, while both EQE and PL are averaging over the bulk of the HaP films. Disorder and defect states at the surface are expected to be enhanced compared to the bulk,[35] which can be expected to result in an increased Urbach energy as measured by PES; ii) the energetic resolution of optical measurements is usually better than the herein used electron energy analyzer resolution of 125 meV. Although this is considered for the modeling, the broadening by the analyzer increases the uncertainty especially for very steep tails;[31] iii) For the CFSYS measurements, the sample has not been exposed to any ambient air and was measured under ultra-high vacuum conditions, whereas most optical spectroscopy measurements are recorded in ambient air. In the next section it will be shown, that on the one side even short exposure to ambient air affects the sample surface, such that the actual valence band structure is smeared out and E_t strongly increased. On the other side, also degradation and enhanced trap state densities upon vacuum storage are observed. As the bulk of the film is expected to be less affected by the exposure to air or vacuum than the surface, the comparison between PES and the optical methods is not straight-forward and deviations between E_t and E_U need to be expected.

In literature, several DFT studies of the dispersion relation for $MAPbI_3$ single crystals can be found.[20,22,23] The angle resolved DFT calculations by Shirayama et al. on $MAPbI_3$ single crystals[22] here assist as an approximated reference to our experimental data, despite the fact, that the obtained

dispersion relation will deviate from the one of the herein used perovskite composition. Philippe et al. compared DFT calculations for $CH_3NH_3PbI_3$ and $CH_3NH_3PbBr_3$ and showed that the uppermost valence bands are dominated by I-related states, whereas the Br-related valence band states are found to be at lower binding energies.[20] Since for the more complex crystal structure of mixed metal-halide perovskites, to our knowledge, no comparable studies are published so far, a comparison to calculations for $CH_3NH_3PbI_3$ is the only option.

According to Shirayama et al., the highest valence band has a global maximum at the R-point in reciprocal space and a second local maximum towards lower binding energies at the M-point with an energetic distance of $E_{V,M} - E_{V,R} = -0.32$ eV.[22]

The two main transitions that we observe in the measured data, and which are modeled by the two polylogarithm functions can be attributed to two different valence band edges, according to the respective parabolic VBM in the dispersion relation. While the attribution of $E_{V,PLog,High}$ to the R-point is reasonable since no energetically higher VBM with significant DOS is measured by CFSYS, the lower VBM with an energetic distance of around - 0.38 eV cannot be assigned with certainty. As in both DFT[22] and angle resolved PES (ARPES)[23] the energetically next lower VBM of $MAPbI_3$ in the dispersion relation is found at the M-point, one could speculate that also for CsMAFA the energetically lower VBM can be attributed to the M-point.

The fact, that we indeed measure the very highest VBM is further supported by the ARPES measurements on $MAPbI_3$ performed by Zu et al.[23], who quantified the VBM at the R-point using a linear extrapolation of the respective ARPES spectrum and found $E_{V,Lin,R} = -1.41$ eV. When aligning their ARPES data to our measured CFSYS spectrum (see Figure S7), our modelled $E_{V,PLog,High}$ is found 70 meV below $E_{V,Lin,R}$ evaluated by Zu et al. and is thus in very good agreement, especially considering that a slightly different material is investigated.

In angle-integrated PES on spin-coated HaPs thin films, where the small crystallites are oriented in arbitrary directions, the detected photo electrons in general originate from the whole Brillouin-zone.[36] In case of any preferential orientation, the different k-vectors might not be weighted equally and suppress or enhance emission in certain directions. While the attribution and correlation to the DFT calculated DOS needs to be taken very carefully, the fact of observing two separate VBM with an energetic distance of around 0.38 eV, most likely resulting from different points in the Brillouin zone can be stated more confidently.

All PES measurements are carried out under illumination, namely by the UV light or X-rays used to excite the measured photoelectrons. In decent photovoltaic absorbers such as our HaPs, this should lead to both, a) a splitting of the quasi Fermi levels (QFLS), and b) a change of band bending due to charge redistribution in the perovskite arising from a combination of inhomogeneous depth profiles of photogeneration, recombination and charge extraction at contacts. Specifically, in our sample structures, photoelectrons are emitted on the front, and holes are extracted through the rear contact. The surface Fermi level that we model, E_F^*, is then the quasi Fermi level of the electrons under measurement illumination conditions: $E_F^* = E_{F,n,front}$. Since our rear contact is a very efficient hole extraction layer, as evidenced both by high solar cell fill factors[8] and in direct measurements[6], we can assume a relatively flat quasi Fermi level of the holes throughout the perovskite film, $E_{F,ITO,back} \approx E_{f,p,rear} \approx E_{f,p,front}$. Thus, $E_{F,ITO} - E_F^*$ is equal to the QFLS between $E_{F,p}$ on the back of the perovskite film and $E_{F,n}$ on its front, i.e. it is the surface photovoltage under these specific illumination conditions.[37] With $E_{V,PLog,High} = -1.41$ eV relative to the surface quasi Fermi level and a band gap of 1.63 eV (also indicated by the sketch of the conduction band in Figure 4), we find the electron quasi Fermi level to be close to the conduction band, which should not be surprising in a highly efficient photoabsorber under illumination.

However, the observed difference of E_F^* - $E_{F,ITO}$ is much less compared to the expected QFLS, which is in the order of several hundreds of meV under these illumination conditions. Thus, a significant drop of $E_{f,n}$ from the illuminated bulk to the surface in combination with a downwards band bending needs to be present. Considering the large amount of defects created under the illumination and the vacuum conditions, affecting the perovskite's surface, such a drop due to recombination at these defects is easily conceivable. It is important to note, again, that we actually observe the Fermi edge of the electrons, E_F^*, while in conventional He-UPS measurements, this edge is not visible because it is below the noise floor. Therefore, E_v from He-UPS is usually reported on the binding energy scale, thus relative to the contact's Fermi level (in our case, this would be $E_{F,ITO}$ on the rear of the sample), which can lead to an unrecognized SPV as a result of quasi Fermi level splitting. Indeed, in some He-UPS measurements, the sample is illuminated with very low photon fluxes in order to minimize this effect as well as changes in band bending.[38] Importantly, SPV and changes in band bending might also occur in other PES measurements, which could be a reason for the widely observed "n-type"-character of the surface of HaPs[37] as well as other inconsistencies e.g. when comparing parameters extracted from XPS and UPS measurements which use very different illumination, thus charge generation conditions.

To sum up the discussion of our modelling approach: We have shown that, with a higher resolution and lower detection limit, two distinct valence band edges can be observed. Different to conventional angle integrated He-UPS, CFSYS can trace the DOS of the very highest VBM, assumed to be at the R-point in reciprocal space from DFT on the similar HaP $MAPbI_3$. The ad-hoc evaluation method of a linear extrapolation on a semi-logarithmic scale has been shown to strongly depend on the detection limit and thus an advanced model was adapted to consistently quantify the VBM. Thus, near-UV high-resolution PES can assist to better understand the valence

band structure of complex multi-cation multi-halide perovskites. Knowing which band edge exactly is experimentally probed by He-UPS and either calculating the energetic distance of the highest VBM to the measured one with the support of DFT calculations, or experimentally determining the energetic distance (e.g. by a method with a low noise floor such as CFSYS) seems to be the most exact approach for determining the Fermi level position in the band gap (as also suggested by Yang and Yang[21]). However, if no high sensitivity PES such as CFSYS is available, support by precise DFT calculations for each specific material might be necessary to assess the position of the highest VBM with high confidence. However, these are very demanding for complex multi cation and multi halide perovskites.

After discussing in detail the energetic positions of an exemplary sample, we want to point out that, even with the very same sample history and material composition, slightly varying values might be obtained. We therefore measured the valence band region for four individual, but nominally identical CsMAFA layers and summarized the obtained fitting parameters in Table 1 (the fitted spectra as well as all obtained fitting parameters can be found in the supporting information, Figure S8 and Table S1, respectively).

Table 1. Obtained fitting parameters for four different CsMAFA ($(Cs_{0.05}(MA_{0.17}FA_{0.83})_{0.95}Pb(I_{0.83}Br_{0.17})_3$) layers with nominally identical processing history.

Sample	Precedent condition	$\Delta E_{V,Plog}$	($E_{V,PLog,High}$ - E_F^*)	(E_F^* - $E_{F,ITO}$)	E_t	D_{it}	D_{it} [a]
		[eV]	[eV]	[eV]	[meV]	[rel. to a_0]	[cm^{-3}]
1	After NUPS meas.	0.38	- 1.41	0.03	43	1.5×10^{-4}	7.9×10^{16}
2	After NUPS meas.	0.39	- 1.50	0.13	48	1.8×10^{-4}	9.2×10^{16}
3	After NUPS meas.	0.38	- 1.42	-0.12	44	3.8×10^{-4}	2.0×10^{17}
4	After NUPS meas.	0.36	- 1.37	-0.17	41	1.3×10^{-4}	6.8×10^{16}
	Mean (±std. dev.)	0.38(1)	- 1.43(5)	-	44(3)	$2(1) \times 10^{-4}$	1.1×10^{17}

[a] The defect density (D_{it}) per volume unit is estimated by normalization based on DFT calculations for $MAPbI_3$.

The energetic position of the highest detectable valence band edge, $E_{V,PLog,High}$, with respect to the surface Fermi level, E_F^*, varies from - 1.37 eV to -1.50 eV with a mean value of – 1.43 eV. The distance from $E_{V,PLog,High}$ to $E_{V,PLog,Low}$, $\Delta E_{V,PLog}$, is consistently about 0.36-0.39 eV. The calculated distance between $E_{V,R}$ and $E_{V,M}$ for $MAPbI_3$ taken from literature, is found to be around 0.32 eV,[21,22] thus slightly below these experimentally found values, which are for CsMAFA. This can be attributed to the different composition of our samples.

As an example, we also modelled the He-UPS spectrum of Sample 2 (which is shown in Figure 2 and Figure 3, see Figure S9 for the modelling) with a polylogarithm function. Because of the different noise level, only the energetically lower VBM can be modeled, and we do not consider any measurement induced broadening. We obtain $E_{V,PLog,Low}$ = -1.9 eV and as $\Delta E_{V,PLog}$ = 0.39 eV is known from the CFSYS modelling, $E_{V,PLog,High}$ = -1.51 eV can be estimated. This is in very good agreement with the values obtained by modelling the CFSYS data. To summarize, the situation for this or closely related materials appears to be as follows: in He-UPS only the region between the very highest and the next lower VBM is visible, whereas the actual VBM itself and an eventual disorder related Urbach tail are hidden below the noise floor. This, in turn, may lead to the extraction of E_F - E_v values which are larger than the bandgap, which are clearly unphysical. In contrast CFSYS clearly reveals the VBM, with a square-root shape as expected from theory for a parabolic band edge.

Turning now to the Fermi level position relative to the substrate Fermi level (E_F^* - $E_{F,ITO}$), a shift of up to 300 meV in between the samples is observed. This however is not attributed to inconsistent modelling, but to a shift of the whole spectrum relative to $E_{F,ITO}$ (see supporting information, Figure S2), which can be attributed to three main reasons:

a) During the measurement, the samples are illuminated by UV-light. Charge carriers that are photogenerated during the measurements lead to a splitting of the quasi Fermi levels, which results in a surface photovoltage (SPV), i.e. a potential difference between the Fermi level positions at the top and the bottom of the layer stack (also indicated in Figure 1). In fact, the situation is similar to a solar cell with the HaP film as the absorber, being held close to open circuit conditions. (Not exactly at V_{oc} conditions, however, since there is a small current flow due to the photoemitted electrons, balanced by the extraction of holes at the SAM/ITO rear contact.) These holes then recombine with electrons supplied through the sample contact. This leads to a charge carrier imbalance across the film, thus a photovoltage.[39] Since these non-intended charge separations happen to a different extent for every sample, also a slightly different SPV $\neq$ 0 eV is expected. Note, that the effect of SPV might be greatly enhanced once an electron selective layer is applied to the front side.[39]

b) Positive charging of the surfaces might occur when photoelectrons are generated at a higher rate than the corresponding states can be refilled by electrons from the sample contact. This leads to a shift of the spectrum towards lower binding energies. From the evaluation of the Pb 4f and I 3d peak position of the XPS spectra, a slight charging was indeed observed with 0.1-0.3 eV for samples 2-4 compared to sample 1 (Figure S10). Since the charging (observed in the core levels with XPS illumination) does not directly correlate to the observed shifts of E_V on the binding energy scale (observed in the VB region with UV illumination) and, at least for sample 4, is even larger than the observed deviation of the surface Fermi level, it cannot be the only reason.

c) The sample surface condition can be different between samples for a variety of reasons. First the processing history, including the solution mixing, spin coating timing, minor changes in the atmosphere surrounding the sample and the sample transfer influence the surface conditions of the

respective sample.[36] Also other mechanisms, such as the usage of DMSO in the solvent mixture of the perovskite are discussed in literature to induce surface trap-states,[15] which influence the Fermi level position in the band gap due to charge redistribution between bands and gap states ("Fermi level pinning"). Additionally, the measurement-induced degradation due to UV-light leads to increased defect densities, which will be discussed in the next section.

Since all these physical reasons (charge carrier generation and separation, charging and Fermi level pinning) shift the spectrum along the binding energy axis, thus relative to $E_{F,ITO}$, it is not possible to distinguish the exact underlying mechanism.

The slope of the exponential tail, quantified by the tail parameter E_t, varies from 41 meV to 48 meV for the four measured samples. The true value might be lower, because the obtained values are at the limit of the energetic resolution with this experimental setup. The shape of the DOS in the valence band should be consistent in between different samples and only shift relative to $E_{F,ITO}$, as elaborated above.

With the low detection limit of CFSYS we are capable of measuring and even quantifying the density of occupied states above the modeled band edges, D_{it}, using a convolution of the gap states DOS modeled as three Gaussian functions (D1-D3), multiplied with the Fermi distribution and convolved with the instrument transfer function. We explicitly do not provide any physical interpretation of the nature or total number of defect bands. Relative to the amplitude scaling parameter, a_0, belonging to $E_{V,PLog,High}$, the defect density varies from $1.3 \cdot 10^{-4}$ to $3.8 \cdot 10^{-4}$ with a mean value of $2.1 \cdot 10^{-4}$. Since the measured internal yield is directly proportional to the density of occupied states, assuming a similar excitation cross section over the whole spectral range, we can obtain a rough estimate for the density of occupied gap states per volume unit by normalizing the internal yield to a known DOS at a defined position. We use the amplitude scaling parameter a_0 of

$E_{V,PLog,High}$ and attribute it to a density of states in the valence band of $5.13 \cdot 10^{20}$ $cm^{-3}eV^{-1}$ as calculated from DFT calculations for $MAPbI_3$ by Shirayama et al.[22] (see Figure S12 for a detailed description). The obtained densities of occupied trap states vary between $6.8 \cdot 10^{16}$ cm^{-3} and $2.0 \cdot 10^{17}$ cm^{-3} with a mean value of $1.1 \cdot 10^{17}$ cm^{-3}. We note that these estimated defect densities are very high considering the high PCE in solar cells obtained with this exact material. Indeed, a combination of several factors may lead to an overestimation of the defect densities found here (10^{16} - 10^{17} cm^{-3}) compared to those reported in literature (10^{13}-10^{16} cm^{-3})[40–43] for high-quality polycrystalline $MAPbI_3$ and CsFAMA films: (1) Depending on the measurement method (e.g. for deep level transient spectroscopy[41] or time-resolved microwave conductivity[42]) the defect density is estimated from modelling recombination processes, which provide an indirect way of determining the defect density also including assumptions about the capture cross section; it can be speculated that even though the defect states are present in the material in the amounts we report on here, their charge carrier capture cross sections could be lower than assumed in the electrical measurements. Thus they would not contribute strongly to trap-assisted non-radiative recombination in the working device; (2) our assumption of a constant matrix element in the studied photon energy range (4-7 eV) might be invalid, and the matrix element decreases significantly as the photon energy increases, implying that the signal in the defect region is "amplified" with respect to the signal originating from the VB;[44] note, that the excitation cross sections for extended (VB) states and localized (defect) states might differ; (3) the obtained defect densities are only relevant to the surface region, and the actual amount in the bulk is much lower;[35] and (4) the actual surface density is further strongly influenced by a variety of sample conditions as well as the measurement itself, which will be discussed in the next section.

4.3 Defect generation upon sample illumination and handling

We proceed by investigating changes in the valence band DOS upon different illumination conditions and sample handling, such as transfer and storing conditions before measurements.

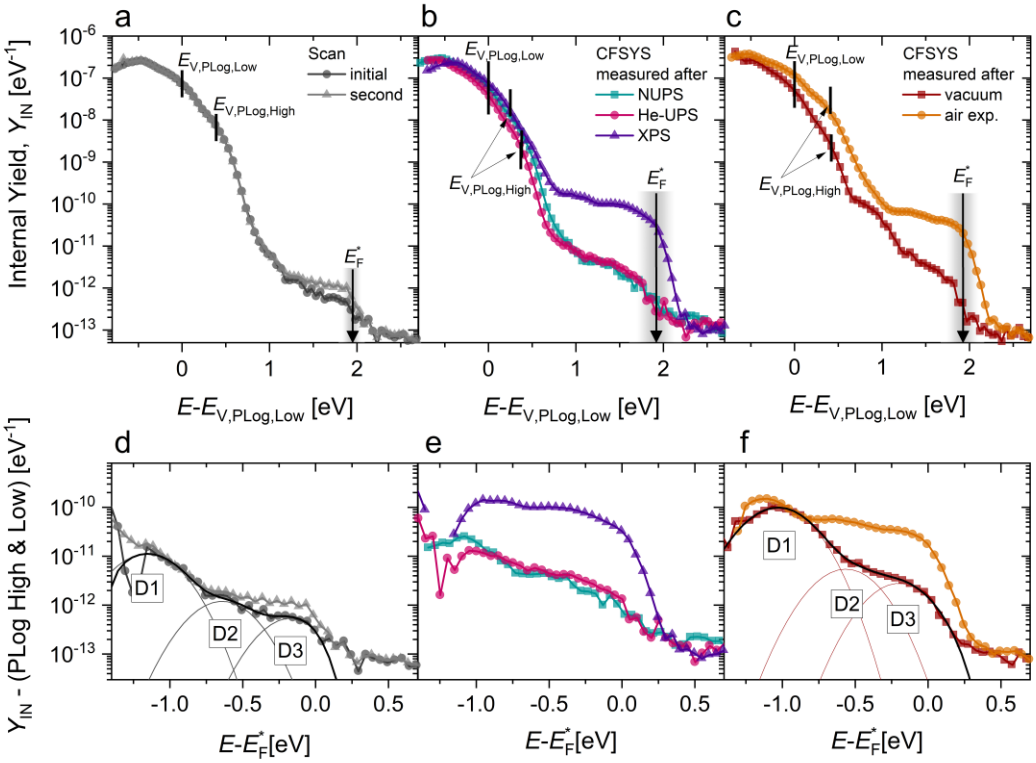

Figure 5. CFSYS spectra of CsMAFA ($(Cs_{0.05}(MA_{0.17}FA_{0.83})_{0.95}Pb(I_{0.83}Br_{0.17})_3$) for different sample histories: a) and d) with two sequential CFSYS scans, b) and e) after measurements with varying illumination (NUPS, He-UPS, XPS), c) and f) after two weeks of vacuum storage and < 10 min exposure to ambient air. a)-c) are the spectra as measured and aligned to the lower valence band edge, $E_{V,PLog,Low}$; d)-f) show the measured internal yield minus the two modeled valence bands aligned to the surface Fermi level, E_F^*.

In Figure 5a-c the spectra of the internal yield for different sample histories are shown. The resulting modelling parameters are summarized in Table 2. The modeled spectra and a detailed comparison of all obtained parameters is shown in the supporting information in Figure S13 and Table S3, respectively. Additionally, we show the residuals of the measured data minus the two polylogarithm functions in Figure 5d-f, aligned to the surface Fermi level, E_F^*. The area under

these residuals is a direct measure of the occupied defect density per volume unit in the band gap and is modeled by the defect peaks D1-D3.

First, we assess the influence of the near UV irradiation during UPS and CFSYS measurements on the valence band region and on defect generation in the band gap. In Figure 5a, the internal yield spectra of two sequential scans obtained from a typical CsMAFA layer (Sample 2 from the previous section) aligned to the modelled $E_{V,PLog,Low}$ are shown. Usually, the sample is first illuminated for the NUPS measurement for 15 min with a photon energy of 6.5 eV, which is necessary to find a suitable final state kinetic energy for the CFSYS measurement. For each CFSYS scan the UV-illumination time is 60 min with photon energies varying from 3.7 eV to 7.3 eV. Considering the fitting results in Table 2, we observe that the high DOS valence band positions ($E_{V,PLog,High}$ and $E_{V,PLog,Low}$) are not affected by this prolonged UV irradiation. In contrast, the slope parameter decreases and the defect density in the energy region of E-E_F^* = -0.6 eV up to the Fermi energy increases with illumination time (see also Figure 5d). The decrease of the slope parameter can be attributed to a change in the energetic position of D1, which is a free parameter of the fit: if the fit shifts D1 towards the valence band edge, it includes more states in the exponential band tail region, which thus can decrease the fitted slope parameter slightly. Considering Peaks D1-D3, between the 1st and 2nd CFSYS scan, the total density of gap states is significantly increased from $1.8 \cdot 10^{-4}$ to $4.6 \cdot 10^{-4}$ relative to a_0 ($9.2 \cdot 10^{16}$ to $2.4 \cdot 10^{17}$ cm^{-3}). However, this is partially attributed to a fitting artifact due to the shift of D1 towards the valence band edge. Considering only D2 and D3, which can be fitted reliably since they are not influenced by the valence band parameters, the increase of the combined gap state density in these peaks is slightly lower with $2.4 \cdot 10^{-5}$, from $2.3 \cdot 10^{-5}$ to $4.8 \cdot 10^{-5}$ relative to a_0 and thus around $1.2 \cdot 10^{16}$ cm^{-3}, and can indeed be attributed to defect generation during the near UV illumination, induced by the

measurement. To investigate the dynamics of the formation of those trap states upon illumination with less pre-assumptions from the advanced modelling of the whole spectrum, CFSYS in a very small photon energy range (4.9 eV to 5.0 eV) was measured repeatedly on a previously not illuminated area of the sample, directly after the transfer into the vacuum system. Immediately after starting the illumination, gap states start to increase by about half an order of magnitude and saturate at an internal yield of $Y_{IN} = 2.5 \cdot 10^{-12}$ eV^{-1} and thus around $3.3 \cdot 10^{16}$ $cm^{-3}eV^{-1}$ after 20 min illumination time (see supporting information, Figure S14a and Figure S14b).

Since all other samples experience initially 15 min of UV irradiation, the formation of the gap states is already close to its saturated value when the CFSYS measurement starts and thus, no difference between scan 1 and 2 is observed for most samples. To confirm that the saturation persists upon longer illumination time, a sequence of 10 scans was performed and no further defect formation could be observed (Figure S14c). This implies that for this specific material an intrinsic gap state density below ~ 10^{16} $cm^{-3}eV^{-1}$ will not be detectable by our CFSYS tool. However, we can approximate the defect densities above this saturated value, while being confident to not further degrade the sample with the irradiation required for the measurement itself. Considering the broadly observed degradation of lead based halide perovskites upon UV-illumination in literature, especially in combination with ETL or HTL materials,[45] the saturation of defect formation as observed here is remarkable.

With its low measurement-induced damage, CFSYS may assist to investigate the degradation of perovskite absorber materials under harsher illumination conditions, such as He-I and X-rays. Figure 5b shows the CFSYS spectra of a CsMAFA film (sample 3), which has been measured after NUPS (same as all samples in the previous section), after He-UPS (21.2 eV, $t_{ill.} = 40$ min) and

after XPS (Al-K_α, 1486.6 eV, $t_{ill.}$ = 3 h). The respective residuals after subtracting both polylogarithm model functions, i.e. the gap states, are shown in Figure 5e.

Table 2: Valence band and defect parameters obtained from fitting our model to CFSYS measured on CsMAFA, $Cs_{0.05}(MA_{0.17}FA_{0.83})_{0.95}Pb(I_{0.83}Br_{0.17})_3$, with different sample histories.

Sample	Sample history	$\Delta E_{V,Plog}$	($E_{V,PLog,High}$ - E_F^*)	(E_F^* - $E_{F,ITO}$)	E_t	D_{it}	D_{it} [a]
		[eV]	[eV]	[eV]	[meV]	[rel. to a_0]	[cm^{-3}]
2	After NUPS meas., initial CFSYS scan	0.39	- 1.50	0.13	48	1.8×10^{-4}	9.2×10^{16}
2	Second CFSYS scan	0.39	- 1.50	0.13	43	4.6×10^{-4}	2.4×10^{17}
3	After NUPS meas.	0.38	- 1.42	-0.12	44	3.8×10^{-4}	2.0×10^{17}
3	After He-UPS meas.	0.37	- 1.46	-0.15	51	3.0×10^{-4}	1.6×10^{17}
3	After XPS meas.	0.25	- 1.65	-0.15	109	7.7×10^{-3}	3.9×10^{18}
-	10 min. air exposure	0.42	- 1.52	-0.15	76	1.2×10^{-3}	6.1×10^{17}
-	Vacuum storage	0.38	- 1.41	-0.13	45	2.2×10^{-3}	1.1×10^{18}

[a] The defect density (D_{it}) per volume unit is estimated by normalization based on DFT calculations for $MAPbI_3$.

The exposure to He-I irradiation had a comparably minor impact on the sample. The observed valence band structure, especially the clear distinction between $E_{V,PLog,High}$ and $E_{V,PLog,Low}$ was maintained, but their energetic distance slightly decreased from 0.38 eV to 0.37 eV. Relative to the substrate Fermi level, $E_{V,PLog,High}$ is shifted towards higher binding energies by 40 meV. E_t also slightly increased from 44 meV to 51 meV, which might indicate partial degradation of the crystal structure. The decreasing total gap state density from $3.8 \cdot 10^{-4}$ to $3.0 \cdot 10^{-4}$ ($2.0 \cdot 10^{17}$ to $1.6 \cdot 10^{17}$ cm^{-3}) is somewhat misleading and again attributed to the energetic position of D1, which moved further away from $E_{V,PLog,High}$. This fitting artefact here leads to a concomitant decrease of its area. Considering the measured spectra in Figure 5b the increase in defect density is better quantified by the area of D2 and D3, which slightly increased from $6.9 \cdot 10^{-5}$ to $8.6 \cdot 10^{-5}$ ($3.6 \cdot 10^{16}$ to $4.4 \cdot 10^{16}$ cm^{-3}) after NUPS and He-UPS, respectively. With this, we can conclude that aside from the possible

damage that may have occurred upon the initial exposure of the sample to UV irradiation, the additional damage induced by additional He-I radiation in the investigated time scale is negligible. This is an important finding, since He-UPS is widely applied as the standard method for valence band spectroscopy.

Exposure to X-Rays for about 3 h however changed the shape of N_{OCC} in the whole valence band region, such that it is hardly possible to model both high DOS valence band maxima as done for all other samples. For both, $E_{V,PLog,High}$ and $E_{V,PLog,Low}$, the energetic position relative to the substrate Fermi level shifted towards higher binding energies and at the same time their energetic distance decreased to 0.25 eV. The exponential tail slope parameter E_t strongly increased to 109 meV, which can be interpreted as a significant structural damage on the sample surface. The density of gap states was also further increased by more than one order of magnitude to $7.7 \cdot 10^{-3}$ ($3.9 \cdot 10^{18}$ cm^{-3}) as compared to after He-I and Near-UV illumination.

The chemical origin of the defect formation might be linked to a combination of several decomposition routes. As discussed by Lin et al. for $CH_3NH_3PbI_3$, two main routes might play a role,[46] where either the material is decomposed into PbI_2 and CH_3NH_3I or into PbI_2 combined with out-gassing of the volatile methylamine and HI species. Then, PbI_2 could be further decomposed into metallic Pb^0 and iodine. Often the appearance of Pb^0-states in the Pb 4f core level is thus used as an indication of degradation in HaP surfaces.[46–48] We also performed XPS measurements and analysis (Figure S10), but no indication of metallic lead could be found in all our samples within the detection limit. We hence conclude that the observed gap states might be attributed to either decomposed perovskite and thus PbI_2, or already show the appearance of a low amount of Pb^0, which is not observable by XPS yet. Since our analyzer is not very sensitive at the high kinetic energies used for XPS, the measurement time of 3 h for all detail spectra is rather long. However,

several studies confirm, that this is still below the X-ray illumination time, where metallic lead could be observed.[46,47] CFSYS measurements on pure PbI_2 confirm that indeed it shows a similar, almost constant defect density in the band gap up to the Fermi level (see Figure S15), which might originate from the lead-iodine composition or already from metallic lead formed by photolysis. In further studies by Wu et al. on lead-iodine based perovskites, a similar distribution of trap states throughout the band gap up to the Fermi level was observed by means of near-UV PES.[16] Our results are proof, that even though no indication of degradation or decomposition of the lead halide perovskites film might be observed by means of XPS, a partial decomposition is to be expected. Further studies, e.g. with varying amounts of excess PbI_2 in the HaP precursor solution, different solvents and compositions as well as systematic variation of X-ray illumination time would be needed for a clear assignment and understanding of those gap states. For example, Zhang et al. investigated the influence of different solvents used in the perovskite precursor solution and found that a chemical reaction between DMSO and methylammonium (MA^+) within the perovskite precursor is linked to the formation of defect states related to DMA^+ and NH_4^+.[15]

Last, we want to discuss the influence of different sample environment conditions: short exposure to air (< 10 min) and storage in vacuum for two weeks. The corresponding spectra shown in Figure 5c and f. While both conditions do not severely affect the high DOS valence band region, as the energetic position relative to the Fermi level as well as the energetic distance between $E_{V,PLog,High}$ and $E_{V,PLog,Low}$ stay almost constant, the DOS in the band tail region as well as the gap state density are very sensitive to those conditions. Interestingly, the short exposure to air led to a similarly severe formation of gap states as the long illumination with X-rays, up to $1.2 \cdot 10^{-3}$ relative to a_0 ($6.1 \cdot 10^{17}$ cm^{-3}), being almost equally distributed up to the Fermi level. Furthermore, the exponential tail slope parameter, E_t, increases significantly to 76 meV. The equal distribution of

the gap states up to the Fermi level and amount of gap states relative to the valence bands at lower binding energy is reminiscent of the spectra obtained by Levine et al. for mixed $APbBr_3$-perovskites,[17] where similarly, the layers have shortly been exposed to ambient air. The interaction of lead halide perovskites with humid air has been shown to enhance the degradation of lead halide pervoskites[49] with again, decomposition into PbI_2 and other species. Thus, observed trap states in HaPs, especially with highly sensitive PES methods, need to be evaluated carefully, and any exposure to air should be avoided. Since the amount of gap states is still below the detection limit of most He-I based PES systems, this conclusion could not be drawn until now.

It is worth paying special attention to the sample, which had been stored in vacuum for two weeks. While for most samples the gap states seem to be rather equally distributed throughout the band gap (up to the Fermi level), here we observe the appearance of a distinct and localized defect band D1 at +0.38 eV relative to $E_{V,PLog,High}$ and the overall defect density was increased to $2.2 \cdot 10^{-3}$ relative to a_0 ($1.1 \cdot 10^{18}$ cm^{-3}). However, the prolonged storage in vacuum did not affect the exponential tail slope, which remained at 45 meV. The volatile methylamine is known to leave the HaP material during annealing at 100°C[48] ("outgassing") and a slowed down, but similar behavior should be expected in ultra-high vacuum.[47] Note, that also in finalized HaP-based solar cells, a degradation in reduced ambient pressure has been observed, and was linked to outgassing and phase separation.[50] Thus, the observed appearance of a distinct defect band might be caused by an intermediate decomposition state induced by prolonged exposure to vacuum conditions, especially in combination with UV-illumination.[51] Further systematic studies will be needed to clarify how the density and energetic position of defects evolve under different environmental conditions.

5. Conclusions

In this study, we applied Near-UV excited constant final state yield spectroscopy (CFSYS) to halide perovskites (HaPs) and systematically determine the valence band edges, as well as investigate the evolution of gap states for the first time systematically and quantitatively. We have demonstrated that CFSYS enables deep insights into the valence band structure of HaPs and can trace the density of occupied states over a high dynamic range of up to seven orders of magnitude.

By comparing CFSYS to conventional He-I and near-UV ($h\nu$ = 6.5 eV) based UPS on CsMAFA ($Cs_{0.05}(MA_{0.17}FA_{0.83})_{0.95}Pb(I_{0.83}Br_{0.17})_3$) metal-halide perovskite thin films, we have demonstrated that a substantial part of the DOS in the valence band region is hidden below the noise floor of conventional He-I UPS. We found that evaluating the leading edge of the energetically highest valence band feature on a semi-logarithmic scale gives inconsistent results, especially when methods with higher signal-to-noise ratio are applied. Additionally, the definition of a consistent energetic position on the exponential tail slope is not possible.

To solve this issue, we proposed a new model to describe the HaPs valence band, considering parabolic band edges and energetic band fluctuations. Until now, only angle-resolved methods could provide information about the strong dispersion of valence bands in HaPs. With our new fitting approach applied to Near-UV CFSYS data, we were able to resolve two features in the valence band DOS, resulting from local maxima at different points in the Brillouin zone, with a mean energetic distance of 0.38 eV, from which only the energetically lower one is observable in classical He-UPS due to the higher density of states. Further, the Fermi edge could directly be observed and thus a reliable energetic position of the valence band edge at -1.50 eV to -1.37 eV relative to the surface Fermi level of the electrons is found for four different samples of CsMAFA. We were able to quantify occupied gap states with a density of states around four orders of magnitude below the density of states at the highest valence band edge, which are partially

generated by the UV-illumination used for the measurements. By normalizing the density of states to DFT calculations of $MAPbI_3$ from literature we could roughly estimate the defect density in volume units to be in the order of ~ 10^{16} cm^{-3}.

Furthermore, we investigated the effect of different sample environments and illumination conditions on the valence band DOS of CsMAFA. We found that near-UV illumination induces a total density of occupied gap states up to a mean value of $2.2 \cdot 10^{-4}$ ($1.1 \cdot 10^{17}$ cm^{-3}), which was not significantly enhanced by further He-I irradiation, while the characteristic energy, describing the slope of the exponential band tail, E_t, slightly increased. X-ray illumination had an enormous impact on the valence band DOS with both a strongly increased density of occupied gap states and increased E_t. Short exposure to ambient air had a similar severe influence on the gap state density, however E_t was less affected. A prolonged storage in ultra-high vacuum mainly led to the appearance of a distinct defect band at +0.38 eV relative to the highest modeled valence band edge with an approximate density of $2 \cdot 10^{-3}$ (10^{18} cm^{-3}).

With the herein provided results, we have demonstrated that CFSYS with Near-UV excitation is a useful and suitable tool to investigate the characteristically low density of states at the valence band edge of HaPs. Even very low electronic defect densities can be directly traced and hence important information about the energetics, as well as a quantification of defects on or close to the HaP film's surface, can be obtained. The lack of similarly sensitive PES measurements, combined with the strong dispersion of HaPs, might partly explain the large spread of energetic values for VBM with respect to the Fermi level found in literature for perovskites and charge-selective layers. The high information depth of several nm will also enable the investigation of buried interfaces as employed in, e.g. carrier selective contacts for perovskite solar cells.

ASSOCIATED CONTENT

Supporting Information. The following files are available free of charge.

Experimental optimization of monochromator entrance/exit slit width; Valence band region of CsMAFA, measured by He-UPS, NUPS and CFSYS; Determination of the Fermi edge by a sigmoidial Boltzmann function; Determination of Urbach energy by photoluminescence and spectral ellipsometry measurements; Comparison of ARPES measurement on MAPbI3 to CFSYS on CsMAFA; Fitting results for CFSYS valence band spectra of CsMAFA; Fitting polylogarithmic model to He-UPS; X-ray photoemission spectroscopy measurements; Normalization of internal yield to density of states; Spectra and Fitting parameters of CsMAFA under different illumination conditions and environmental conditions; Generation of gap states in CsMAFA upon near-UV illumination; (PDF)

AUTHOR INFORMATION

Corresponding Author

*E-Mail: korte@helmholtz-berlin.de

Author Contributions

The manuscript was written through contributions of all authors. All authors have given approval to the final version of the manuscript.

Notes

The authors declare no competing financial interest.

ACKNOWLEDGMENT

The authors acknowledge funding from the Federal Ministry of Education and Research (BMBF) for funding of the Young Investigator Group Perovskite Tandem Solar Cells within the program "Materialforschung für die Energiewende" (grant no. 03SF0540), the Helmholtz Association within the HySPRINT Innovation lab project, and the HyPerCells joint Graduate School. This research was supported by the joint agreement between the DAAD (German Academic Exchange Service) and FONDECYT (National Fund for Scientific, Technological Development and Technological Innovation) under the agreements 57508544 DAAD and 423-2019-FONDECYT. Further support has been provided by the PUCP vice chancellorship for research (VRI, Project No. CAP-2019-3-0041/702). The authors thank Thomas Lußky for technical support and Bor Li for part of the sample preparation. I.L. thanks the PEROSEED project and AiF project (ZIM-KK5085302DF0) for financial support, and David Cahen and Isaac Balberg for fruitful discussions.

REFERENCES

(1) Matsushima, T.; Bencheikh, F.; Komino, T.; Leyden, M. R.; Sandanayaka, A. S. D.; Qin, C.; Adachi, C. High Performance from Extraordinarily Thick Organic Light-Emitting Diodes. *Nature* **2019**, *572* (7770), 502–506. https://doi.org/10.1038/s41586-019-1435-5.

(2) Dagar, J.; Fenske, M.; Al-Ashouri, A.; Schultz, C.; Li, B.; Köbler, H.; Munir, R.; Parmasivam, G.; Li, J.; Levine, I.; Merdasa, A.; Kegelmann, L.; Näsström, H.; Marquez, J. A.; Unold, T.; Többens, D. M.; Schlatmann, R.; Stegemann, B.; Abate, A.; Albrecht, S.; Unger, E. Compositional and Interfacial Engineering Yield High-Performance and Stable p-i-n Perovskite Solar Cells and Mini-Modules. *ACS Appl. Mater. Interfaces* **2021**, *13* (11), 13022–13033. https://doi.org/10.1021/acsami.0c17893.

(3) Tong, J.; Jiang, Q.; Zhang, F.; Kang, S. B.; Kim, D. H.; Zhu, K. Wide-Bandgap Metal Halide Perovskites for Tandem Solar Cells. *ACS Energy Lett.* **2021**, *6* (1), 232–248. https://doi.org/10.1021/acsenergylett.0c02105.

(4) Jošt, M.; Bertram, T.; Koushik, D.; Marquez, J. A.; Verheijen, M. A.; Heinemann, M. D.; Köhnen, E.; Al-Ashouri, A.; Braunger, S.; Lang, F.; Rech, B.; Unold, T.; Creatore, M.; Lauermann, I.; Kaufmann, C. A.; Schlatmann, R.; Albrecht, S. 21.6%-Efficient Monolithic Perovskite/Cu(In,Ga)Se2 Tandem Solar Cells with Thin Conformal Hole Transport Layers for Integration on Rough Bottom Cell Surfaces. *ACS Energy Lett.* **2019**, *4* (2), 583–590. https://doi.org/10.1021/acsenergylett.9b00135.

(5) Todorov, T.; Gershon, T.; Gunawan, O.; Lee, Y. S.; Sturdevant, C.; Chang, L.-Y.; Guha, S. Monolithic Perovskite-CIGS Tandem Solar Cells via In Situ Band Gap Engineering. *Adv. Energy Mater.* **2015**, *5* (23), 1500799. https://doi.org/10.1002/aenm.201500799.

(6) Al-Ashouri, A.; Magomedov, A.; Roß, M.; Jošt, M.; Talaikis, M.; Chistiakova, G.; Bertram, T.; Márquez, J. A.; Köhnen, E.; Kasparavičius, E.; Levcenco, S.; Gil-Escrig, L.; Hages, C. J.; Schlatmann, R.; Rech, B.; Malinauskas, T.; Unold, T.; Kaufmann, C. A.; Korte, L.; Niaura, G.; Getautis, V.; Albrecht, S. Conformal Monolayer Contacts with Lossless Interfaces for Perovskite Single Junction and Monolithic Tandem Solar Cells. *Energy Environ. Sci.* **2019**, *5* (6), 1035. https://doi.org/10.1039/c9ee02268f.

(7) Mailoa, J. P.; Bailie, C. D.; Johlin, E. C.; Hoke, E. T.; Akey, A. J.; Nguyen, W. H.; McGehee, M. D.; Buonassisi, T. A 2-Terminal Perovskite/Silicon Multijunction Solar Cell Enabled by a Silicon Tunnel Junction. *Appl. Phys. Lett.* **2015**, *106* (12), 121105. https://doi.org/10.1063/1.4914179.

(8) Al-Ashouri, A.; Köhnen, E.; Li, B.; Magomedov, A.; Hempel, H.; Caprioglio, P.; Márquez, J. A.; Vilches, A. B. M.; Kasparavicius, E.; Smith, J. A.; Phung, N.; Menzel, D.; Grischek, M.; Kegelmann, L.; Skroblin, D.; Gollwitzer, C.; Malinauskas, T.; Jošt, M.; Matič, G.; Rech, B.; Schlatmann, R.; Topič, M.; Korte, L.; Abate, A.; Stannowski, B.; Neher, D.; Stolterfoht, M.; Unold, T.; Getautis, V.; Albrecht, S. Monolithic Perovskite/Silicon Tandem Solar Cell with 29% Efficiency by Enhanced Hole Extraction. *Science* **2020**, *370* (6522), 1300–1309. https://doi.org/10.1126/science.abd4016.

(9) Eperon, G. E.; Leijtens, T.; Bush, K. A.; Prasanna, R.; Green, T.; Wang, J. T.-W.; McMeekin, D. P.; Volonakis, G.; Milot, R. L.; May, R.; Palmstrom, A.; Slotcavage, D. J.; Belisle, R. A.; Patel, J. B.; Parrott, E. S.; Sutton, R. J.; Ma, W.; Moghadam, F.; Conings, B.; Babayigit, A.; Boyen, H.-G.; Bent, S.; Giustino, F.; Herz, L. M.; Johnston, M. B.; McGehee, M. D.; Snaith, H. J. Perovskite-Perovskite Tandem Photovoltaics with Optimized Band Gaps. *Science* **2016**, *354* (6314), 861–865. https://doi.org/10.1126/science.aaf9717.

(10) McMeekin, D. P.; Sadoughi, G.; Rehman, W.; Eperon, G. E.; Saliba, M.; Hörantner, M. T.; Haghighirad, A.; Sakai, N.; Korte, L.; Rech, B.; Johnston, M. B.; Herz, L. M.; Snaith, H. J. A Mixed-Cation Lead Mixed-Halide Perovskite Absorber for Tandem Solar Cells. *Science* **2016**, *351* (6269), 151–155. https://doi.org/10.1126/science.aad5845.

(11) Saliba, M.; Matsui, T.; Seo, J.-Y.; Domanski, K.; Correa-Baena, J.-P.; Nazeeruddin, M. K.; Zakeeruddin, S. M.; Tress, W.; Abate, A.; Hagfeldt, A.; Grätzel, M. Cesium-Containing Triple Cation Perovskite Solar Cells: Improved Stability, Reproducibility and High Efficiency. *Energy Environ. Sci.* **2016**, *9* (6), 1989–1997. https://doi.org/10.1039/C5EE03874J.

(12) National Renewable Energy Laboratory, Best Research-Cell Efficiency Chart www.nrel.gov/pv/cell-efficiency.html (accessed 2021 -08 -31).

(13) Zhang, F.; Silver, S. H.; Noel, N. K.; Ullrich, F.; Rand, B. P.; Kahn, A. Ultraviolet Photoemission Spectroscopy and Kelvin Probe Measurements on Metal Halide Perovskites: Advantages and Pitfalls. *Adv. Energy Mater.* **2020**, 1903252. https://doi.org/10.1002/aenm.201903252.

(14) Endres, J.; Egger, D. A.; Kulbak, M.; Kerner, R. A.; Zhao, L.; Silver, S. H.; Hodes, G.; Rand, B. P.; Cahen, D.; Kronik, L.; Kahn, A. Valence and Conduction Band Densities of States of Metal Halide Perovskites: A Combined Experimental–Theoretical Study. *J. Phys. Chem. Lett.* **2016**, *7* (14), 2722–2729. https://doi.org/10.1021/acs.jpclett.6b00946.

(15) Zhang, F.; Hamill, J. C.; Loo, Y.; Kahn, A. Gap States in Methylammonium Lead Halides: The Link to Dimethylsulfoxide? *Adv. Mater.* **2020**, *32* (42), 2003482. https://doi.org/10.1002/adma.202003482.
(16) Wu, X.; Trinh, M. T.; Niesner, D.; Zhu, H.; Norman, Z.; Owen, J. S.; Yaffe, O.; Kudisch, B. J.; Zhu, X.-Y. Trap States in Lead Iodide Perovskites. *J. Am. Chem. Soc.* **2015**, *137* (5), 2089–2096. https://doi.org/10.1021/ja512833n.
(17) Levine, I.; Shimizu, K.; Lomuscio, A.; Kulbak, M.; Rehermann, C.; Zohar, A.; Abdi-Jalebi, M.; Zhao, B.; Siebentritt, S.; Zu, F.; Koch, N.; Kahn, A.; Hodes, G.; Friend, R. H.; Ishii, H.; Cahen, D. Direct Probing of Gap States and Their Passivation in Halide Perovskites by High-Sensitivity, Variable Energy Ultraviolet Photoelectron Spectroscopy. *J. Phys. Chem. C* **2021**, acs.jpcc.0c11627. https://doi.org/10.1021/acs.jpcc.0c11627.
(18) Sebastiani, M.; Di Gaspare, L.; Capellini, G.; Bittencourt, C.; Evangelisti, F. Low-Energy Yield Spectroscopy as a Novel Technique for Determining Band Offsets: Application to the c-Si(100)/a-Si:H Heterostructure. *Phys. Rev. Lett.* **1995**, *75* (18), 3352–3355. https://doi.org/10.1103/PhysRevLett.75.3352.
(19) Korte, L.; Laades, A.; Schmidt, M. Electronic States in A-Si:H/c-Si Heterostructures. *J. Non-Cryst. Solids* **2006**, *352* (9), 1217–1220. https://doi.org/10.1016/j.jnoncrysol.2005.10.046.
(20) Philippe, B.; Jacobsson, T. J.; Correa-Baena, J.-P.; Jena, N. K.; Banerjee, A.; Chakraborty, S.; Cappel, U. B.; Ahuja, R.; Hagfeldt, A.; Odelius, M.; Rensmo, H. Valence Level Character in a Mixed Perovskite Material and Determination of the Valence Band Maximum from Photoelectron Spectroscopy: Variation with Photon Energy. *J. Phys. Chem. C* **2017**, *121* (48), 26655–26666. https://doi.org/10.1021/acs.jpcc.7b08948.
(21) Yang, M.-F.; Yang, J.-P. Revealing Mechanism of Obtaining the Valence Band Maximum via Photoelectron Spectroscopy in Organic Halide Perovskite Single Crystals. *Appl. Phys. Lett.* **2020**, *117* (7), 071602. https://doi.org/10.1063/5.0016223.
(22) Shirayama, M.; Kadowaki, H.; Miyadera, T.; Sugita, T.; Tamakoshi, M.; Kato, M.; Fujiseki, T.; Murata, D.; Hara, S.; Murakami, T. N.; Fujimoto, S.; Chikamatsu, M.; Fujiwara, H. Optical Transitions in Hybrid Perovskite Solar Cells: Ellipsometry, Density Functional Theory, and Quantum Efficiency Analyses for CH3NH3PbI3. *Phys. Rev. Appl.* **2016**, *5* (1), 1–25. https://doi.org/10.1103/PhysRevApplied.5.014012.
(23) Zu, F.; Amsalem, P.; Egger, D. A.; Wang, R.; Wolff, C. M.; Fang, H.; Loi, M. A.; Neher, D.; Kronik, L.; Duhm, S.; Koch, N. Constructing the Electronic Structure of CH3NH3PbI3 and CH3NH3PbBr3 Perovskite Thin Films from Single-Crystal Band Structure Measurements. *J. Phys. Chem. Lett.* **2019**, *10* (3), 601–609. https://doi.org/10.1021/acs.jpclett.8b03728.
(24) Kraut, E. A.; Grant, R. W.; Waldrop, J. R.; Kowalczyk, S. P. Precise Determination of the Valence-Band Edge in X-Ray Photoemission Spectra: Application to Measurement of Semiconductor Interface Potentials. *Phys. Rev. Lett.* **1980**, *44* (24), 1620–1623. https://doi.org/10.1103/PhysRevLett.44.1620.
(25) Guerra, J. A.; Tejada, A.; Korte, L.; Kegelmann, L.; Töfflinger, J. A.; Albrecht, S.; Rech, B.; Weingärtner, R. Determination of the Complex Refractive Index and Optical Bandgap of CH3NH3PbI3 Thin Films. *J. Appl. Phys.* **2017**, *121* (17). https://doi.org/10.1063/1.4982894.
(26) Stolterfoht, M.; Caprioglio, P.; Wolff, C. M.; Márquez, J. A.; Nordmann, J.; Zhang, S.; Rothhardt, D.; Hörmann, U.; Amir, Y.; Redinger, A.; Kegelmann, L.; Zu, F.; Albrecht, S.;

Koch, N.; Kirchartz, T.; Saliba, M.; Unold, T.; Neher, D. The Impact of Energy Alignment and Interfacial Recombination on the Internal and External Open-Circuit Voltage of Perovskite Solar Cells. *Energy Environ. Sci.* **2019**, *12* (9), 2778–2788. https://doi.org/10.1039/C9EE02020A.

(27) Winer, K.; Ley, L. Surface States and the Exponential Valence-Band Tail in a-Si:H. *Phys. Rev. B* **1987**, *36* (11), 6072–6078. https://doi.org/10.1103/PhysRevB.36.6072.

(28) Guerra, J. A.; Tejada, A.; Töfflinger, J. A.; Grieseler, R.; Korte, L. Band-Fluctuations Model for the Fundamental Absorption of Crystalline and Amorphous Semiconductors: A Dimensionless Joint Density of States Analysis. *J. Phys. D: Appl. Phys.* **2019**, *52* (10), 105303. https://doi.org/10.1088/1361-6463/aaf963.

(29) Urbach, F. The Long-Wavelength Edge of Photographic Sensitivity and of the Electronic Absorption of Solids. *Phys. Rev.* **1953**, *92* (5), 1324–1324. https://doi.org/10.1103/PhysRev.92.1324.

(30) Korte, L.; Schmidt, M. Investigation of Gap States in Phosphorous-Doped Ultra-Thin a-Si:H by near-UV Photoelectron Spectroscopy. *J. Non-Cryst. Solids* **2008**, *354* (19–25), 2138–2143. https://doi.org/10.1016/j.jnoncrysol.2007.09.010.

(31) Korte, L. Die Elektronische Struktur Des Silizium-Heterostruktur-Kontakts. Dissertation, Phillips-Universität Marburg, Marburg/Lahn, 2006.

(32) Seah, M. P. The Quantitative Analysis of Surfaces by XPS: A Review. *Surf. Interface Anal.* **1980**, *2* (6), 222–239.

(33) Zu, F.; Wolff, C. M.; Ralaiarisoa, M.; Amsalem, P.; Neher, D.; Koch, N. Unraveling the Electronic Properties of Lead Halide Perovskites with Surface Photovoltage in Photoemission Studies. *ACS Appl. Mater. Interfaces* **2019**, *11* (24), 21578–21583. https://doi.org/10.1021/acsami.9b05293.

(34) Ledinský, M.; Schönfeldová, T.; Holovsky, J.; Aydin, E.; Hajkova, Z.; Landová, L.; Neykova, N.; Fejfar, A.; De Wolf, S. Temperature Dependence of the Urbach Energy in Lead Iodide Perovskites. *J. Phys. Chem. Lett.* **2019**, *10*. https://doi.org/10.1021/acs.jpclett.9b00138.

(35) Ni, Z.; Bao, C.; Liu, Y.; Jiang, Q.; Wu, W.-Q.; Chen, S.; Dai, X.; Chen, B.; Hartweg, B.; Yu, Z.; Holman, Z.; Huang, J. Resolving Spatial and Energetic Distributions of Trap States in Metal Halide Perovskite Solar Cells. *Science* **2020**, *367* (6484), 1352–1358. https://doi.org/10.1126/science.aba0893.

(36) Béchu, S.; Ralaiarisoa, M.; Etcheberry, A.; Schulz, P. Photoemission Spectroscopy Characterization of Halide Perovskites. *Adv. Energy Mater.* **2020**, *10* (26), 1904007. https://doi.org/10.1002/aenm.201904007.

(37) Schroder, D. K. Surface Voltage and Surface Photovoltage: History, Theory and Applications. *Meas. Sci. Technol.* **2001**, *12* (3), R16–R31. https://doi.org/10.1088/0957-0233/12/3/202.

(38) Zu, F.-S.; Amsalem, P.; Salzmann, I.; Wang, R.-B.; Ralaiarisoa, M.; Kowarik, S.; Duhm, S.; Koch, N. Impact of White Light Illumination on the Electronic and Chemical Structures of Mixed Halide and Single Crystal Perovskites. *Adv. Opt. Mater.* **2017**, *5* (9), 1700139. https://doi.org/10.1002/adom.201700139.

(39) Hellmann, T.; Das, C.; Abzieher, T.; Schwenzer, J. A.; Wussler, M.; Dachauer, R.; Paetzold, U. W.; Jaegermann, W.; Mayer, T. The Electronic Structure of MAPI-Based Perovskite Solar Cells: Detailed Band Diagram Determination by Photoemission Spectroscopy

Comparing Classical and Inverted Device Stacks. *Adv. Energy Mater.* **2020**, *10* (42), 2002129. https://doi.org/10.1002/aenm.202002129.
(40) Levine, I.; Gupta, S.; Bera, A.; Ceratti, D.; Hodes, G.; Cahen, D.; Guo, D.; Savenije, T. J.; Ávila, J.; Bolink, H. J.; Millo, O.; Azulay, D.; Balberg, I. Can We Use *Time-Resolved* Measurements to Get *Steady-State* Transport Data for Halide Perovskites? *Journal of Applied Physics* **2018**, *124* (10), 103103. https://doi.org/10.1063/1.5037637.
(41) Heo, S.; Seo, G.; Lee, Y.; Lee, D.; Seol, M.; Lee, J.; Park, J.-B.; Kim, K.; Yun, D.-J.; Kim, Y. S.; Shin, J. K.; Ahn, T. K.; Nazeeruddin, M. K. Deep Level Trapped Defect Analysis in $CH_3NH_3PbI_3$ Perovskite Solar Cells by Deep Level Transient Spectroscopy. *Energy Environ. Sci.* **2017**, *10* (5), 1128–1133. https://doi.org/10.1039/C7EE00303J.
(42) Hutter, E. M.; Eperon, G. E.; Stranks, S. D.; Savenije, T. J. Charge Carriers in Planar and Meso-Structured Organic–Inorganic Perovskites: Mobilities, Lifetimes, and Concentrations of Trap States. *J. Phys. Chem. Lett.* **2015**, *6* (15), 3082–3090. https://doi.org/10.1021/acs.jpclett.5b01361.
(43) Siekmann, J.; Ravishankar, S.; Kirchartz, T. Apparent Defect Densities in Halide Perovskite Thin Films and Single Crystals. *ACS Energy Lett.* **2021**, 3244–3251. https://doi.org/10.1021/acsenergylett.1c01449.
(44) Jackson, W. B.; Kelso, S. M.; Tsai, C. C.; Allen, J. W.; Oh, S.-J. Energy Dependence of the Optical Matrix Element in Hydrogenated Amorphous and Crystalline Silicon. *Phys. Rev. B* **1985**, *31* (8), 5187–5198. https://doi.org/10.1103/PhysRevB.31.5187.
(45) Farooq, A.; Hossain, I. M.; Moghadamzadeh, S.; Schwenzer, J. A.; Abzieher, T.; Richards, B. S.; Klampaftis, E.; Paetzold, U. W. Spectral Dependence of Degradation under Ultraviolet Light in Perovskite Solar Cells. *ACS Appl. Mater. Interfaces* **2018**, *10* (26), 21985–21990. https://doi.org/10.1021/acsami.8b03024.
(46) Lin, W.-C.; Lo, W.-C.; Li, J.-X.; Wang, Y.-K.; Tang, J.-F.; Fong, Z.-Y. In Situ XPS Investigation of the X-Ray-Triggered Decomposition of Perovskites in Ultrahigh Vacuum Condition. *npj Mater. Degrad.* **2021**, *5* (1), 13. https://doi.org/10.1038/s41529-021-00162-9.
(47) McGettrick, J. D.; Hooper, K.; Pockett, A.; Baker, J.; Troughton, J.; Carnie, M.; Watson, T. Sources of Pb(0) Artefacts during XPS Analysis of Lead Halide Perovskites. *Mater. Lett.* **2019**, *251*, 98–101. https://doi.org/10.1016/j.matlet.2019.04.081.
(48) Philippe, B.; Park, B.-W.; Lindblad, R.; Oscarsson, J.; Ahmadi, S.; Johansson, E. M. J.; Rensmo, H. Chemical and Electronic Structure Characterization of Lead Halide Perovskites and Stability Behavior under Different Exposures—A Photoelectron Spectroscopy Investigation. *Chem. Mater.* **2015**, *27* (5), 1720–1731. https://doi.org/10.1021/acs.chemmater.5b00348.
(49) Shirayama, M.; Kato, M.; Miyadera, T.; Sugita, T.; Fujiseki, T.; Hara, S.; Kadowaki, H.; Murata, D.; Chikamatsu, M.; Fujiwara, H. Degradation Mechanism of CH3NH3PbI3 Perovskite Materials upon Exposure to Humid Air. *J. Appl. Phys.* **2016**, *119* (11). https://doi.org/10.1063/1.4943638.
(50) Jiang, Y.; Yang, S.-C.; Jeangros, Q.; Pisoni, S.; Moser, T.; Buecheler, S.; Tiwari, A. N.; Fu, F. Mitigation of Vacuum and Illumination-Induced Degradation in Perovskite Solar Cells by Structure Engineering. *Joule* **2020**, *4* (5), 1087–1103. https://doi.org/10.1016/j.joule.2020.03.017.
(51) Zu, F.; Schultz, T.; Wolff, C. M.; Shin, D.; Frohloff, L.; Neher, D.; Amsalem, P.; Koch, N. Position-Locking of Volatile Reaction Products by Atmosphere and Capping Layers Slows

down Photodecomposition of Methylammonium Lead Triiodide Perovskite. *RSC Adv.* **2020**, *10* (30), 17534–17542. https://doi.org/10.1039/D0RA03572F.

For Table of Contents Only